Theoretical and experimental modeling of local scale CO_2 flushing of hydrous rhyolitic magma.

Simakin A.G.[1], Devyatova V.N.[1] and Shiryaev A.A.[2]
[1]IEM RAS, Chernogolovka
[2]IPCE RAS, Moscow

Submitted to RJES 23.03.2023

Abstract

Flushing of hydrous silicic magmas with crustal carbonic fluid may be an important factor controlling the explosiveness of rhyolitic eruptions. We present combined theoretical and experimental study of the interaction of carbonic fluid with a hydrous silicic melt. The process of diffusional equilibration of a CO_2 bubble with a silicic melt was simulated numerically in the spherical approximation. The rapid water transfer from the melt to the bubble is followed by a slower diffusion of CO_2 into the melt. The water distribution becomes almost uniform over a period proportional to the diffusional unit of time $0.14\tau_W$, determined by the initial inter-bubble distance W and the water diffusion coefficient D_w ($\tau_W = W^2/D_w$), while the CO_2 distribution remains strongly contrasting. This process was modelled experimentally with a hydrous albite melt at P=200 MPa and T=950-1000°C. In the first series of experiments at T=950°C, a glass powder was filled with pure CO_2 at the beginning of the experiment, forming numerous bubbles at the run temperature. Micro-FTIR measurements showed that after 40 minutes the water content decreased from 4.9 down to 1.8 wt.% with the maximum CO_2 content 500 ppm. After 4 hours, the crystallinity increases to 85%, and the fluid bubbles almost disappear. The second series of experiments CO_2 interacted with a 2 mm high column of hydrous albite melt. Diffusion profiles in the quenched glass were measured using EMPA (H_2O) and micro-FTIR (CO_2 and H_2O). The estimated diffusion coefficients for H_2O (1.1×10^{-6} cm^2/s) and CO_2 ($1.5e\times10^{-7}$ cm^2/s) are consistent with published data. Scaling analysis predicts that in natural environment the homogenization of water in rhyolitic magma after an influx of CO_2 bubbles few millimeters in size lasts for 1-30 days, i.e. a period compatible with pre-eruptive processes in a magma chamber.

Key words. Carbon dioxide, explosive volcanic eruption, experiment in IHPV, diffusion of CO_2 and H_2O, magma flushing with CO_2.

Introduction

Intra-chamber degassing caused by CO_2 flushing at a mid-crustal depth can be an essential factor determining the explosive style of basic magmas eruption [*Dallai et al., 2011*]. Using geochemical and petrological tools, it is possible to distinguish the invasion of CO_2 into the magma from the assimilation of carbonate, causing the CO_2 generation in near-surface conditions by the CaO input [*Mollo et al., 2010*]. While processes involving carbonic fluid at the mid-crustal depths can only be studied indirectly, a high flux of CO_2 of deep origin is measured at the surface in mantle plume settings (Yellowstone [*Werner and Brantley, 2003; Lowenstern, Hurwitz, 2008*], Iceland [*Barry et al., 2014*], Canary Islands [*Longpré et al., 2017*]) and some subduction zones (Italy [*Frezzotti et al., 2010*]). CO_2 is formed in the upper mantle during decarbonization reactions [*Frezzotti and Touret, 2014*] and can be transported to the crust either by dissolution in the basic magma or along with it via deep tectonic dislocations (shear zones). During the upward migration, this fluid may cross magma chambers. The interaction of the carbonic fluid and water-bearing magmas can be equally important for basaltic and silicic compositions [*Caricchi et al., 2018*]. Upon interaction with CO_2, the water undesaturated melt reaches saturation with respect to the CO_2-H_2O composite fluid. In addition to simple recharging, intra-chamber vesiculation may be a factor increasing the magma pressure in the chamber to a level sufficient to cause failure of the chamber roof and onset of an explosive eruption. The carbonic fluid transfers heat and dissolved components, thereby affecting the heat budget of the magma and its composition [*Simakin and Ghassemi, 2018*].

Melt inclusions (MIs) in quartz provide a unique opportunity to obtain direct information about the fluid regime of magma in the chamber and during the ascent of magma before the eruption. Quartz protects MI better than, for example, olivine from the loss of volatiles (especially water) at high temperatures during the flow of magma and after the eruption. However, on a daily-weekly scale, water and some elements (Li) can escape from the MI in quartz. Selected MIs without water loss or corrected data characterize well the climatic eruptions of Yellowstone. On Figure 1 points of H2O and CO2 content form subvertical arrays, starting from compositions poor in CO2 and undersaturated with water, extended vertically to solubility isobars of 200–250 MPa. The Lava Creek Tuffs MIs exhibits water content variation in the range 3-4 wt.% [*Befus and Gardner, 2016*], while the Huckleberry Ridge Tuff MIs have higher water concentrations of 4-5 wt.% [*Myers et al., 2016*].

Usually, such subvertical trends are interpreted as a manifestation of degassing due to depressurization. Figure 1 shows the calculated sequences of compositions of melts formed at pressure drops from 200 to 5 MPa in closed and open system modes [*Newman, Lowenstern, 2002*]. The interaction of CO_2-enriched fluid with magma (or flushing) also leads to degassing or dehydration of the melt, increasing the volume of the fluid phase. Assuming local equilibrium, as

in modeling a pressure drop-induced degassing path, melt compositions will follow a solubility isobar as shown by the thick grey line in Figure 1, with compositions directed towards increasing CO2 content. The same line with compositions directed towards increasing water content will characterize the process of magma crystallization with exsolution of excess fluid [Wallace et al., 1995]. These trends are far from those observed for the Yellowstone eruptions data.

The interaction of a water saturated high-silica rhyolite melt with a CO_2 bearing (X_{CO2}=0.4) fluid at T=800°C and P=100 MPa was experimentally studied by *Yoshimura and Nakamura* [*2010*]. Under the experimental conditions, the used bubble-free water-saturated glass slab had a highly viscous (>10^5 Pa·s) and was partially dehydrated from the entire surface. In three-hour experiments, the H_2O concentration became uniform within a 0.5 mm thick melt volume, while the CO_2 distribution was still far from saturation. Disequilibrium effects were also observed during vesiculation after decompression of a melt saturated with CO_2 and H_2O, caused by slower diffusion of CO_2. Delayed saturation of the melt with CO2 after dehydration can cause the melt compositions to follow the trend shown by the solid purple line marked by the upward arrow in Figure 1. In their vertical parts, the trends of equilibrium decompression degassing and disequilibrium CO2 flushing are quite similar, which, at least requires not to ignore the possibility of the later process. Additional information, such as the isotopic composition (δ^7Li, δ^{11}B, δ^{34}S) [*Gurenko et al., 2021; Neukampf et al., 2022; Zelenski et al., 2022*] which is affected by isotope fractionation during degassing, could potentially help in choosing between these alternative mechanisms.

The dehydration of magma caused by CO_2 flushing leads to an increase in the liquidus temperature of magmatic minerals. This effect causes crystallization at a significant rate, exceeding the rate of quasi-equilibrium crystallization, due to the slow cooling of large volumes of magma beyond the reach of the geothermal circulation. Decompression degassing produces a similar effect of magma crystallization with an increase in undercooling, which has been well studied experimentally [*Simakin et al., 1999; Couch et al., 2003*].

Here we present the results of the experiments in an internally heated high pressure vessel (IHPV) of the interaction of CO_2 with a hydrous albite melt, extending the results obtained by *Yoshimura and Nakamura* [*2010*]. Our experiments include studying the effect of albite crystallization caused by dehydration of the melt with CO_2 fluid. The results of numerical modeling of the growth of CO_2 bubbles during melt dehydration are also presented, which allow us to extend the experimental results to natural conditions with larger bubbles and a low fluid volume content.

Part 1 Numerical modeling of hydrous melt flushing with CO_2 on a single bubble level

The model

The interaction of a CO_2-enriched fluid with a hydrous melt (flushing) can be easily modelled theoretically in the equilibrium approach, similarly to the degassing process of a magma saturated with a two-component fluid. It is sufficient to know the mutual solubility of CO_2 and H_2O in a melt of given composition. An explosive eruption can start at a high rate on a time scale of hours or days. In this case, slow process of diffusive bubble growth can control compositions of the fluid and the adjacent melt. There are many approximate analytical and fully numerical solutions for diffusive equilibration (growth or dissolution) of a bubble in a melt [e.g., *Navon et al., 1998*]. For clarity and consistency of consideration, we briefly describe the problem and methods of its solution.

Let us start with an analysis of the complete equation of diffusive mass transfer around a bubble growing in an infinite volume of the melt. The growing bubble expands and causes a radial flow of the melt with a rate (for the spherically symmetric case) *U(r)*. Therefore, the diffusion equation for any component of the melt can be written as:

$$\frac{\partial C}{\partial t} = -U(r)\frac{\partial C}{\partial r} + \frac{1}{r^2}(\partial(D(C)r^2\left(\partial C/\partial r\right))/\partial r), \qquad (1)$$

where D(C) is the diffusion coefficient. In a narrow concentration range one can use the diffusion coefficient at an average concentration C^* and thus omit the nonlinear term $dD(C)/dC\,(\partial C/\partial r)^2$:

$$\frac{\partial C}{\partial t} = -U(r)\frac{\partial C}{\partial r} + D(C^*)\left(\frac{2\,\partial C/\partial r}{r} + \frac{\partial^2 C}{\partial r^2}\right) (2)$$

The radial flow rate *U(r)* is given by:

$$U(r) = \frac{U_0 r_0^2(t)}{r^2} \quad (3),$$

here $r_0(t)$ is the bubble radius at the moment *t*. A set of bubbles of the equal size is usually [e.g., *Coumans et al., 2020*] modeled in a spherical melt shell geometry. In this approximation, both the inner and outer (midpoint between neighboring bubbles) boundaries move as the bubble expands. The bubble growth rate is controlled by the diffusive flux of main component:

$$U_0 = \rho_m/\rho_{fl} D_w \frac{\partial C(r,t)}{\partial r}\Big]_{r=r0(t)} \qquad (4)$$

The influence of the flow is defined by the parameter $R\rho=\Delta C\rho_m/\rho_{fl}$, where ΔC is the characteristic concentration difference $\Delta C = C_{r=r0}-C_0$ (e.g., 0.01). It can be shown that for moderate values of $R\rho$ <1 (pressures >100 MPa), the advection term can be omitted. At low pressures and fluid density, the parameter $R\rho$>>1, and advection strongly affects the concentration field and transforms the solution to the type of a narrow boundary layer [*Zelenski*

et al., 2021]. Here we consider processes of the melt-fluid exchange in the magma chamber at a typical depth of about 7 km (P=200 MPa) with $R\rho \approx 0.1$ with a weak effect of advection. Our fluid consists of two main components CO_2 and H_2O, so two diffusive mass fluxes act on the bubble volume and the boundary condition (4) is replaced by:

$$\frac{dV_{bub}}{dt} = \frac{dm_{co2}/dt + dm_{H2O}/dt}{\rho_{fl}(X)} + \frac{d\rho_{fl}/dt}{\rho_{fl}^2}\left((1-X)\frac{dm_{co2}}{dt} - X\frac{dm_{H2O}}{dt}\right), \quad (5),$$

where m_{CO2} and m_{H2O} are the masses of the components in the bubble, X is the mole fraction of CO_2 in the fluid, ρ_{fl} is the fluid density depending on its composition at fixed P and T. The concentrations of H_2O and CO_2 in the melt at the bubble boundary are assumed to be in equilibrium with the fluid composition:

$$C_{i,m}(r=r_0)=F_i(X), \text{ where } i=CO_2, H_2O \qquad (6)$$

Material parameters.

Diffusion coefficients for CO_2 and H_2O are taken from [*Zhang and Ni, 2010*]. At T=850-1000°C, P=200 MPa and Cw=4-5 wt.% the ratio D_{H2O}/D_{CO2} is in the range 4-10.

The CO_2-H_2O fluid density was calculated from the model from [*Kerrick and Jacobs, 1981*]. We approximated $\rho_{fl}(X_{CO2})$ and d $\rho_{fl}(X_{CO2})/dX$ for T=850°C and P=200 MPa by a second order polynomial.

The solubility of H_2O (C in wt.%, P in kbar) was approximated as:

$$C_{H2O} = 4.1(P(1- X_{CO2})^{1.35})^{1/2} \quad (8)$$

and CO_2 (C in wt.%, T in °C):

$$C_{CO2} = 0.0592\, kX_{CO2}^{0.79},\ k=-0.54013 + 0.00164T, \quad (9)$$

where X_{CO2} is the mole fraction of CO2 in the fluid. These approximations correspond to experimental data for pressures 75 MPa < P < 500 MPa, generalized for rhyolite in [*Botcharnikov et al., 2005*].

Method of solution.

The equation (2) was transformed to a dimensionless form by applying a linear scale equal to the initial bubble radius R_0 and a time scale t_0 related to the diffusion coefficient of water $t_0=R_0^2/D_{H2O}$. The problem under consideration is characterized by two dimensionless parameters: $R\rho$ (see above) and $D_x = D_{H2O}/D_{CO2}$. For the numerical solution for the radial distributions of H_2O and CO_2 we use the Lagrange formulation for spatial dimension, i.e. each node moves at the melt velocity [*Zelenski et al., 2021*]. The global inverse square approximation [*Cheng et al., 2003*] of the concentration fields allows gridless computation:

$$\hat{C} = \sum_1^n \alpha_i \frac{1}{\sqrt{r_i^2 + c^2}} \quad (7),$$

where the constant c is chosen empirically and depends on the distance between nodes. The error of the solution strongly depends on the value of the coefficient c that regulates the extent of the influence of each node. Diffusion equations for CO_2 and H_2O are rigorously formulated by applying differential operators to the approximation of the concentrations by Eqn. (7). Since the flow is weak, the nodes experience small displacements, and no new nodes should be generated, as in the case of large $R\rho$.

Results

The calculations are carried out at D_x=6, $R\rho$=0.046 and several initial volume fractions of fluid $\varepsilon_0=(R_0/R_1)^3$=0.005; 0.033; 0.053. The time-successive radial profiles of water concentration in the melt at $\varepsilon = 0.033$ are shown in Figure 2 a,b. Water migrates into the bubble, so its concentration in the melt decreases from 5 wt.% to 4.3 wt.%. A steep gradient of water concentration at τ=0.5 evolves almost to a flat one at τ=5. At the same time, CO_2 migrates into the melt. The concentration gradient is still steep at τ=5. In Figure 3, the distributions CO_2(r) and H_2O(r) are shown on the $CO_2(H_2O)$ plot. In this diagram, the distributions evolve from a steep concave curve to an almost vertical line (τ>3-4). With an order of magnitude decrease in the volume fraction of bubbles, the time of homogenization of the water content increases by $\sim\varepsilon_0^{2/3}$ times, which is expected from the scaling relations. Figure 3 shows that the CO_2 content in the fluid, reflected by the maximum CO_2 content in the melt, increases with the volume fraction of the bubbles.

At short times, when the diffusion front is far from the outer boundary, the radial distribution of the i-th volatile component can be described by a simple analytical solution in dimensionless coordinates $\xi = r/r_0$, $\tau = tD_i/r_0^2$. Here, we neglect the change in the boundary concentration, which depends on the composition of the fluid, and advection:

$$C(r,t) = c_0 + \frac{\Delta C}{\xi} erfc\left(\frac{\xi - 1}{2\sqrt{\tau}}\right) \quad (10)$$

Obviously, at τ→∞ ($erfc(0)$=1) the distribution described by Eqn. (10) becomes a widely used stationary function $C(r,t) = \Delta C r_0/r$. Formally, the Eqn. (10) is a solution of the diffusion equation with an initial stepwise distribution: $C(r>r_0,0)=c_0$; $C(r=r_0,0)=\Delta C$. However, the solutions of the diffusion equation weakly depend on the initial conditions. In particular, if the boundary condition in time-dependent ($\Delta C = \Delta C(t)$), the distribution $C(r,t)$ is approximated by Eqn. (10) at a sufficiently slow change in the concentration at the boundary. As can be seen in Figure 3, the numerical and simplified theoretical dependences of $CO_2(H_2O)$ for a dimensionless

time of 0.5 are quite close, which confirms the possibility of simple calculation of this dependence for various diffusion coefficients.

The ideal case of fluid exchange considered above may be far from those observed in nature, where the interaction of unevenly distributed moving bubbles with a fluid enriched in CO_2 and a hydrous melt occurs along with crystallization caused by dehydration. In the second part of the article, we report experimental results on CO_2 dehydration of albite melt, often taken as a model of silicic magmas, and consider these effects.

Part 2 Experimental modeling of crystallization induced by CO_2 flushing

Process of the bubble-magma interaction modelled above is only possible for a superheated magma. The interaction of hydrous albite melt at high temperatures with CO_2 generated *in situ* by interaction with calcite, was studied experimentally in [*Simakin et al., 2012*]. The water content drops by 2 wt.% in several hours of flushing with CO_2 bubbles. Convection of albite melt at the millimeter scale caused by bubbles was observed. Natural melts are usually in equilibrium with one or more crystalline phases. The extraction of water by CO_2-rich bubbles induces their crystallization, since the loss of water increases the liquidus temperatures of magmatic minerals. The crystallization complicates simple process of diffusive fluid-magma interaction. We model this process in a simple albite-H_2O system at near liquidus temperature. In one series of the experiments, CO_2 bubbles with a characteristic inter-bubble distance of several tens of microns interacted with a hydrous albite melt. In the second series, the volume of albite melt interacted with the carbonic fluid via the upper interface to model the process on a larger linear scale of several millimeters.

Experimental technique and methods.

The experiments employing double capsule technique were carried out in Pt-capsules at IHPV (UHPG-10000 type) at IEM RAS and were terminated by isobaric quenching at a rate of 100–250°C/min, and at 60°/sec in some runs. The starting hydrous albite glass was produced from crystalline albite (natural mineral from Kalba, Kazakhstan) at T=1200°C and P=200 MPa for 5 hours with the addition of a desired water content. To homogenize the water distribution, the glass was powdered and remelted at the same parameters. According to the Karl Fisher Titration (KFT) data, the water content in the starting albite glass was 4.9 ± 0.1 and 5.1± 0.1 wt % in the two series of experiments. Determination of the water content in the first glass by FTIR method gives a slightly lower value of 4.7± 0.1 wt %.

In the first series of experiments, albite glass was a 100–200 μm powder, obtained by sieving and placed in a larger capsule. AgC_2O_4 loaded into a smaller capsule was used as a source of CO_2, in an amount providing a glass/ CO_2 weight ratio of ~5. The small capsule (3 mm diameter) with the squeezed open end was placed in a large one (5 mm diameter), which was welded.

In the second series of experiments, glass cylinders were tightly inserted into the small capsules. The source of CO_2 was a mixture of $CaCO_3$ and quartz in an amount providing a glass/ CO_2 weight ratio of ~1/2.5. To accelerate the decarbonization reaction with the formation of CO_2, a small amount of Na_2CO_3 or K_2CO_3 was added. The mixture was loaded into a large open capsule and covered with a separating platinum cap. Then a small capsule with a piece of glass was placed on the lid and the large capsule was welded. While using the cylindrical pieces of aluminosilicate glass, the fluid interacted with a melt through a sharp interface. Taking into account the curvature of the interface due to the capillary effect, this setting approximates a bubble in the melt with a size of several millimeters, which is consistent with real magmatic systems. On the contrary, in runs with the starting glass powder, due to the large number of bubbles, the reactions are complete in a short time. The experimental conditions, including temperature and duration, are shown in the Table 1.

Weighing was done in an AUW220D analytical balance (Japan), with a measurement accuracy of ±0.1 mg for the mass range used. The composition of the run products were studied by SEM-EDS on a Tescan VEGA II XMU electron scanning microscope equipped with EDX analyzer with a Si(Li) INCA Energy 450 solid-state detector. The analysis was performed at an accelerating voltage of 20 kV. The obtained data were processed using the INCA Suite ver. 4.15 software with subsequent recalculation of the obtained results for weight contents using software packages developed by A.N. Nekrasov at IEM RAS. The Tescan Atlas program was used to process the BSE images and determine the phase proportions. The water content was analyzed using the Karl-Fisher titration (KFT) on an AQUQ 40 device with a heating module for solids. According to the instrument calibration data, the accuracy of water determination is 3 rel. %. The Raman spectra of fluid from bubbles in experimental glasses were measured on a RM1000 spectrometer equipped with CCD detector, rejection filter, and Leica microscope. The spectra were excited using 532 nm solid-state diode laser. The laser beam was focused on a sample with 50× objective. The measurement parameters are as follows: laser power 22 mW, slit width 50 μm, and counting time 5×10 s.

The local content of water and CO_2 was measured on a Nicolet iN10 FTIR microscope equipped with a liquid nitrogen cooled MCT detector. The microscope and sample compartment were continuously purged with high purity dry nitrogen prior to and during the acquisition of the

spectra. The measurements were performed in transmission mode at room temperature; the samples were carefully cleaned in acetone and placed on a KBr plate. The microscope was focused on the top surface of the sample. For the profiles, an aperture of 50 × 50 μm^2; the measurement spots were immediately adjacent to each other. The spectra were obtained in the spectral range 600–6000 cm^{-1}. At least 64 scans were recorded per spectrum with a spectral resolution of 2 cm^{-1}. The FTIR spectra were processed using the Origin 9.5 software. Basic nonlinear correction was performed for each region of interest.

The interpretation of IR spectra requires additional information. Water contents were calculated from the combination 4500 cm^{-1} and 5200 cm^{-1} bands for hydroxyl and molecular water, respectively. The corresponding linear extinction coefficients and density of the albite glass were taken from [*Behrens et al, 1996*]. The signal of molecular CO_2 in IR spectrum at ~2349 cm^{-1} is superposed on a gaseous CO_2 doublet present as a trace despite the purging. The rotational bands of the dissolved CO_2 are suppressed. The spectral envelope was deconvoluted into three Gaussian components. After the deconvolution the contribution of atmospheric CO_2 peaked at 2336 and 2361 cm^{-1}. Carbon dissolved in the glass is also present as a carbonate ion. An isolated symmetrical CO_3^{2-} ion has an active IR asymmetric stretching mode ν_3 at 1415 cm^{-1}. Adsorbed CO_3^{2-} is characterized by the splitting of this band into two with a separation $\Delta\nu_3$, reflecting interaction with the substrate: weakly monodentate and strongly adsorbed bidentate CO_3^{2-} ions are assigned to $\Delta\nu_3$=100 and 300 cm^{-1}, respectively [*Coenen et al., 2018*]. In hydrous albite glass, one band at ≈1610 cm^{-1} overlaps with OH-bending mode of molecular water at ~1636 cm^{-1}. Subsequently, another band of the CO_3^{2-} doublet at 1375 cm^{-1} was used in the analysis. The extinction coefficients for molecular CO_2 and CO_3^{2-} were taken from [*Stolper et al., 1987*]. CO_2 dissolves in albite melt mainly in the form of molecular CO_2. The fraction of the carbonate form increases with cooling and in quenched glass depends on the glass formation temperature T_g. *King and Holloway* [*2002*] used $r=CO_{2,mol}/(CO_{2,mol}+ CO_{2,carb})$=0.9 in their analysis. Application of the thermodynamic model from [*Konschak and Keppler, 2014*] to our data at T_g=600°C gives r=0.73. At low total carbon ($CO_{2\ tot}$) the carbonate band at 1375 cm^{-1} is poorly resolved and the $CO_{2,tot}$ was estimated from data on molecular CO_2 corrected with r=0.8 and 0.73.

Results of experiments.

The first set of experiments was performed at P=200 MPa and T=950°C. AgC_2O_4 used as the fluid source decomposes 100-200 °C below softening of the Ab glass. CO_2 fills the pores and forms bubbles when the glass powder melts. BSE and optic images showed that the bubbles are

50-200 μm in diameter with a population of tiny bubbles few microns in size. Volume fractions of both types of the bubbles are shown in Table 1 in columns ε_{fl1} and ε_{fl2}, respectively. Over time, the bubbles quickly evolved from the melt (see Table 1), assuring CO_2 flushing.

The local water content of the vesiculated glass was estimated using EMPA. The concentrations of all elements, including oxygen (with the exception of hydrogen), were measured by focusing the electron beam on a 10x10 μm^2 square. This method reproduces well the KFT value of 5.1 wt. % in the starting glass. Minimum water content drops to 2.5-2.6 wt.% in 30 min experiment (Table 1) and to 2.7-2.8 wt.% at 40 min duration. The Table 1 shows values corrected for crystals present in the sampled areas. The minimum water content in the glass can be estimated based on the composition of the fluid (column $X_{CO2,min}$ in Table 1), assuming that all water has partitioned into the fluid. The values of $X_{CO2,min}$ in different runs differ slightly due to the variation in the mass ratio of the glass and $Ag_2C_2O_4$. During the crystallization of albite glass, the water content in the melt cannot exceed $C_{w,max}$=3.5 wt.%, at which the run temperature T=950°C is equal to the melting temperature of albite at P=200 MPa (calculated based on the data from [*Holland and Powell, 2001*]). All values of the water content estimated with EMPA are in the range $X_{CO2,min}$<Cw< $C_{w,max}$, except for run a15. During the albite crystallization, water is released, which partially compensates its transfer to the CO_2-enriched fluid. Since the samples from the first set of experiments contain a large number of crystals and bubbles, it is difficult to use the micro-FTIR method to accurately analyze the H_2O and CO_2 content. Several measurements were performed only for glass a21 from a short run. IR spectroscopy gives a water content in the range 1.8-4.2 wt. %, which is consistent with the results of EMPA (see Table 1 and Figure 4). The lowest value of C_w 1.8 wt. % corresponds to the equilibration of the water content with bulk interaction of the fluid with the melt without crystallization. In two analytical points, the content of water and carbon dioxide fall on the solubility curve within the measurement uncertainty. Compositions at the remaining three points are undersaturated with CO_2.

In the first series of experiments, the fluid composition in the bubbles was characterized by the Raman spectroscopy. CO_2 was identified by the characteristic Fermi dyad at 1385 and 1281 cm^{-1} (see Figure 5f) Density of the fluid (ρ_{fl}) in the bubbles was estimated from the difference of positions of these bands (the dyad splitting Δ, cm^{-1}). Since the spectral resolution of the Raman spectra is 1.5 cm^{-1}, exact positions of the bands maxima were determined from approximation of the peaks with a Lorentzian lineshape as recommended in [*Yamamoto and Kagi, 2006*]. The empirical relationship $\rho_{fl}(\Delta)$ from *Wang et al., [2011]* was used. The CO_2 density in the bubbles was evaluated in the samples a20 and a17, showing a rapid increase in the crystallization degree with an increase in the run duration from 75 to 204 minutes, respectively (see Table 1). The

obtained values are 0.566 ±0.01 g/cm^3 (n=3) and 0.673±0.006 g/cm^3 (n=3) for a20 and a17, respectively. The CO_2 density in bubbles in the quenched glass carries information about composition (H_2O/CO_2 ratio) of the fluid at the parameters of the experiment; however, the interpretation of these data, complicated by numerous factors, is beyond the scope of our work.

In the shortest experiment (a21) the albite crystallization caused by dehydration was confined the former boundaries of glass powder chips (Figure 5a). These surfaces were exposed to CO_2 at the beginning of the experiment prior to the melting, and it is likely that microcrystals could have nucleated there and continued to grow at high temperature. The crystals possess a highly elongated morphology. The length of the crystals at 30 min is 15 μm, at 40 min - 24.3 μm. With an increase in the experiment duration to 2 hours, the crystallization degree reaches 80-85 vol. %. These observations correspond to the albite growth rate of about 1.3e-08 m/sec, which is almost two orders of magnitude higher than the growth rate of feldspar from rhyolite melt under similar conditions [*Simakin and Chevychelov, 1995; Rusiecka and Baker, 2021*], which is slowed by diffusion in the melt.

Homogeneous nucleation in albite melt is extremely difficult to achieve, making this composition ideal for glass formation [*Zanotto and Cassar, 2017*]. In our case, the glass powder with a high surface area interacted with CO_2 at temperatures below T_g, which led to the formation of numerous nucleation centers. Since the growth rate is high, the dehydrated albite glass crystallized efficiently. The volume fraction of crystals (ε_s) increases with time as indicated in Table 1 and shown in Figure 5a-d. The transformation kinetics can be approximated with Johnson–Mehl–Avrami–Kolmogorov (JMAK) equation $\varepsilon_s = 1 - a \cdot \exp(-(k \cdot t)^n)$ [e.g., *Yinnon and Uhlmann, 1983*]. The model with n=3 and a=1 characterizing the growth of crystals on preexisting nuclei formed on the surface of glass particles at low temperatures, does not fit the data (Figure 6). The proportion of solids extrapolated to the beginning of the experiment is non-zero (coefficient a less than 1). The best fit model has a value of n=10.5, much larger than the maximum theoretical value of n=4. This implies violation of the constant nucleation rate assumption underlying the JMAK equation. The extremely high rate of transformation in the time interval of 180–250 min may be associated with the rapid delayed homogeneous nucleation during this period. With more data available, the transformation kinetics can be approximated by a sum representing a set of nucleation events with different delay times [*Narine et al., 2006*].

The second set of experiments aimed to reproduce the scenario with a large inter-bubble distance and large bubbles. The carbonic fluid was in contact with a few mm thick volume of hydrous albite at the capsule bottom. At temperature T=1020°C an unexpected mechanism of the interaction between CO_2 and albite melt was observed. In a short experiment a57 (duration 53

min) the distribution of water was estimated using EMPA and is shown in Figure 7. The water concentration at the upper boundary of the profile was $C_w \approx 2$ wt.%. Since the starting glass for this experiment contains many microbubbles, only one measurement of the water content at the boundary was performed using μ-FTIR, which gives $C_w = 2.3$ wt.%. These values are much higher than $C_w \approx 0.2$ wt.%, corresponding to the equilibrium solubility in the fluid with $X_{CO2} \geq 0.9$. More accurate data for both H_2O and CO_2 (Figure 8) were obtained using μ-FTIR for the run ab63 performed under the same PT conditions with bubble-free starting glass (see Table 1 and Figure 5e). The water contents at the boundary of 2.01 and 1.66 wt.% is close to 2-2.3 wt.% at the boundary in run a57. It is noteworthy that the CO_2 content near the contact is significantly smaller than the saturation level expected for a fluid with a high CO_2 mole fraction. As seen in Figure 4, the pair of concentrations (C_{H2O}, C_{CO2}) near the contact with the fluid for the run a63 does not approach the saturation curve for P=200 MPa, in contrast to the data presented in [*Yoshimura and Nakamura, 2010*].

Since there were no signs of crystallization visible on the SEM and optical images in the contact area, we assume that the dense CO_2 fluid interacted with the melt surface and extracted mainly Na and Al, enriching the upper melt film with silica. To explain the observations, the concentration gradients in this protective film must be very high, and the diffusion coefficients must be several orders of magnitude lower than in the albite melt. This hypothesis was tested using experimental data on the diffusion coefficients of CO_2 and H_2O in silica glass [*Behrens, 2010*]. It was found that a silica glass film about 2 μm thick will provide the concentrations and the diffusion fluxes observed on the melt surface in run a63.

Another unusual feature of the mechanism of interaction between albite melt and pure CO_2 at high temperatures is the decrease of the water content in the melt the near the capsule walls in the run 63. From the μ-FTIR data (Figure 8) it can be noted that the water content decreases towards the bottom and that the second, incomplete, profile is characterized by lower concentrations, since it was closer to the wall. At the same time, the CO_2 distributions follow the same dependence with a monotonously decreasing concentration with distance from the contact. These observations can only be explained by the action of some mechanism of ultrafast surface diffusion of water, but not of CO_2, along the Pt-melt interface. This mechanism equalizes the boundary concentration of water with values near the active upper contact with the fluid.

At a lower temperature of 975°C (runs a67 and a68) crystallization began (Figure 5d) from the upper surface and, in some places, near the bottom of the capsule. In this case, the concentration of water in the contact with the crystallization front was estimated only with EMPA at the level of 3.0±0.5 wt.%, which is close to the water content of 3.1 wt. % in albite melt in equilibrium with crystalline albite under experimental PT conditions. The minimum

growth rate of albite, calculated assuming zero nucleation delay time, is 0.9×10^{-8} m/sec (run ab68-4) and 0.98×10^{-8} m/sec (run ab67), which is somewhat lower than the estimate of 1.3×10^{-8} m/sec obtained in the first series of experiments. It can be noted that the composition of alkali feldspars in the runs ab68 and ab67 slightly differ in potassium content with K_2O=0.35±0.1 wt.% and 0.11±0.1 wt.%, respectively. This difference is explained by the use of K_2CO_3 and Na_2CO_3 to stimulate the generation CO_2 in the reaction of $CaCO_3$ with SiO_2 in runs ab68 and ab67, respectively.

We model the distribution of water measured in run a57 by solving 1-D diffusion equation with a variable diffusion coefficient:

$$\frac{\partial C(x,t)}{\partial t} = \frac{\partial D}{\partial C}\left(\frac{\partial C}{\partial x}\right)^2 + D\frac{\partial^2 C}{\partial x^2} \quad (11)$$

The diffusion front of dehydration in this run did not reach the lower boundary of the melt. Therefore, a constant water content of 4.9 wt.% at the bottom and 2 wt.% on the surface were taken as boundary conditions. The diffusion coefficient in silicic melts varies by about half an order of magnitude due to change in the water content, is a function of temperature, composition, and C_{H2O} [*Zhang and Ni, 2010*]. The Equation (11) was solved numerically using the MAPLE 9.5. The data of low-precision EMPA measurements are relatively well reproduced both at concentration dependent and calculated at C_w=4 wt.% values of the diffusion coefficient (Figure 7). The distribution of water in the run a63 is three-dimensional due to the loss of water from the entire surface of the melt and a large diffusion time (dimensionless τ>5). For the run a63 only the CO_2 distribution was considered due to its 1-D character since the influx of CO_2 occurs only from the upper contact of the fluid with the melt (Figure 8b). The CO_2 diffusion coefficient obtained by fitting with a complementary error function (erfc), is 1.5×10^{-7} cm^2/s, which is equal to the value calculated from the model from [*Zhang and Ni, 2010*] at C_{H2O} =4 wt.%.

The distributions of water and carbon dioxide are projected onto the graph (C_{H2O}, C_{CO2}) in Figure 4. On this plot the studied case of extreme dehydration with pure CO_2 at a high mass ratio of CO_2/melt is characterized by a convex path that deviates significantly from the predicted series of concave trajectories evolving towards a vertical line (see Figure 3 and in [*Yoshimura, Nakamura, 2010*]). In our case, it should have a maximum CO_2 content approaching 1000 ppm and a H_2O concentration of less than 1 wt. %. As mentioned above, the influence of the protective film and ultrafast diffusion of H_2O along the Pt-melt interface leads to the observed CO_2(H_2O) trajectory configuration.

Application to rhyolitic magma

Scaling

Schematic diagram showing principle parameters of the CO_2 flushing process in our numerical modeling, experiments with albite melt and in natural environments with initial bubble radius R_0 and inter-bubble distance $W=2R_1$ is shown in Figure 9. Several lines of constant initial volume fraction of fluid ε_{fl} are plotted on this figure to delineate the parametric area expected in nature, encountered in experiments with albite melt and used in numerical modeling. In the process of the water migration in the melt, the water diffusion time scale is $\tau_w = R_0^2/D_w$. As demonstrated above, homogenization of the melt in H_2O takes 4 -20 τ_w depending on the inter-bubble distance $W=2R_1$ or equivalent bubbles volume fraction $0.005<\varepsilon_{fl}< 0.05$. Our modeling data correspond to a simple dependence for the homogenization time $\tau_H=0.55\,\tau_w\varepsilon_{fl}^{2/3}$. After substituting the expression for $\varepsilon_{fl}=(R_0/R_1)^3=8(R_0/W)^3$ into the expression for τ_H, we get $\tau_H=0.138W^2/Dw$. In the first series of experiments with albite melt homogenization time τ_H is 3-10 minutes (see Figure 9). The residence time of bubbles in the melt in these experiments depends on their size, distance from the surface, and the local melt viscosity. The volume fraction of large bubbles rich in CO_2 over time is well described ($R^2=0.9995$) by the exponential function $\varepsilon_{fl}=0.06+0.34exp(-t/t_0)$ with t_0=19 minutes. This means that some bubbles may leave the melt before equilibration even in terms of water distribution. The duration of experiment a21 is comparable to the expected time of water homogenization. The duration of other experiments is several times longer, albite crystallization and diffusive migration of the exsolved water occurred on the scale of the entire sample with water loss through the surface.

In the transition to nature, we marked in Figure 9 τ_H values equal 1 day and 1 month, calculated for rhyolitic magma at T=800°C and C_w=4 wt.%. When a particular geologic process has a time scale greater than τ_H, the local water distribution will be homogeneous. The minimum time for bubbles to escape from the magma due to Stokes flow τ_{St} is proportional to the ratio of the typical width of the convective boundary layer of 1 m [*Simakin and Bindeman, 2022*] to the Stokes bubble rise velocity $U_{st}=1/3(\rho_m-\rho_{fl})gR_0^2/\eta$. Figure 9 shows the Stokes times equal to one month (vertical dashed lines) calculated for albite melt with Cw=4 wt.% at T=800°C and rhyolitic magma (larger values of viscosity and R_0) with the same parameters with the model [*Hui and Zhang , 2007*]. For real values of R_0 and ε_{fl} $\tau_{St}>\tau_H$, so we expect local homogenization of water concentration corresponding to local values of ε_{fl}. Since diffusion of CO_2 is 6-10 times slower, the melt can be dehydrated, but not saturated with CO_2. For sufficiently large bubbles in the rhyolitic magma chambers, the local time of water homogenization becomes compatible with the typical time scale of pre-eruption processes, i.e. in the days-month range.

Discussion

The unexpectedly low concentration of CO_2 and high concentration of H_2O at the contact between CO_2 and hydrous albite melt, observed in our experiments (Figure 7,8), measured with resolution of micro-FTIR method of about 50 μm and resolution of EMPA method of about 5 μm, we explained by the presence of ultrahigh concentration gradients in a narrow boundary layer, which we could not resolve. Under the PT conditions of run a63, the diffusion coefficient of H_2O decreases only by a factor of 5 when the water content in the albite melt decreases from 4 wt.% to zero [*Zhang and Ni, 2010*]. This means that the width of the diffusion zone in albite melt with a decrease in water concentration from 2 wt.% to zero should be only a few times narrower than when falling from 3.5 wt.% to 2 wt.% (≈1000 μm), and can be resolved using available analytical methods. The formation of a near-surface layer of a contrasting composition rich in SiO_2 with high viscosity and low diffusivities during the extraction of Na_2O and Al_2O_3 with CO_2 fluid can explain the observations. Direct experimental measurements of the solubility of the main and trace elements of the melt in supercritical CO_2 under high PT conditions have not been carried out. Observations of CO_2 fluid inclusions contained in pyroxenes indicate high solubility of Al_2O3, Na_2O, K_2O, Rb_2O, SrO and other oxides at a pressure of about 1 GPa and a temperature of about 1000°C [*Berkesi et al., 2012; Hidas et al., 2010*]. Our hypothesis is worth testing, since the likely effect of a protective film can significantly affect estimates of the rate of exchange of hydrous magma with pure CO_2 in nature.

The albite crystals grown in our experiments had a strongly elongated and sometimes even curved morphology (see Figure 5a-d), reflecting strong undercooling that occurs during melt dehydration. In nature, when the composition of the melt is in a quartz field, the formation of non-equilibrium morphologies of quartz crystals is expected in a dehydrated melt. As established experimentally, the transition from flat faceted to skeletal morphology of quartz occurs at DT≈ 55°C [*Swanson and Fenn, 1986*]. Quartz crystals from the large (climatic) explosive eruptions (LCT, Yellowstone; Toba Tuff, Indonesia; Oruanui Tuff, New Zealand) of rhyolitic magma have reentrants, i.e., deep glass embayments open towards the edge of the crystal [*Befus and Manga, 2019; Ruefer et al., 2021*]. Their origin may be related to the non-equilibrium growth stage of quartz with skeletal morphology. The experiments did not confirm the hypothesis that reentrants can be formed during the dissolution of quartz in a magmatic melt, since the experimental dissolution front is flat [e.g., *Acosta-Vigil et al., 2006*]. Some of reentrants were partially or completely filled with fluid, raising the question of how the magma became bubbly at the storage depth before the eruption [*Befus and Manga, 2019*]. Flushing with CO_2 can saturate the magma with the H_2O-CO_2 fluid and make it bubbly. An alternative mechanism is slow fractional

crystallization caused by cooling of the magma, when excess fluid is exsolved [*Wallace et al., 1995*].

Pichavant et al. [*2013*] extended the study of *Yoshimura and Nakamura* [*2010*] by experimental modelling the degassing of a basaltic melt initially saturated with CO_2 and water at P=200 MPa. They found that when the pressure is reduced to 25-50 MPa at a sufficiently low bubble number density (large inter bubble distance), a high supersaturation of CO_2 develops in the melt, while the water content follows equilibrium solubility (Figure 9). As with flushing, CO_2 and H_2O are decoupled due to their contrasting diffusivities. The control of the inter-bubble distance on CO_2 equilibration is very similar to the condition of disequilibrium Cpx growth in the Ab-Di-H_2O system [*Simakin and Devyatova, 2020*]. Non-equilibrium hopper morphology of the crystal rim develops during quenching, when inter-crystalline distances exceed 5-8 μm. At a number density of crystals above $8\text{-}10\times10^9$ cm^{-3}, the diffusion of SiO_2 (the slowest component) homogenizes the melt composition to close to equilibrium. The diffusion coefficient of SiO_2 is many orders of magnitude lower than that of CO_2, so the threshold bubble number density is about 10^4 times lower than that of crystals. In *Pichavant et al.* [*2013*] study, the threshold bubble number density is determined by the time scale of experiments equal to $\tau_{exp}=\Delta P/(dP/dt)$ = 1000-4000 sec. The diffusion coefficient of CO_2 in basalt melt at T=1150°C is 1.3e-07 cm^2/s, and the homogenization time $\tau_{co2} = W^2/D_{co2}$. The condition $\tau_{exp} << \tau_{Dco2}$ (compare with Figure 8) requires the bubble volume number density $N \approx 1/(W/2)^3 << (1.4\text{-}12)10^6$ cm^{-3}, which corresponds to the experimentally estimated $N<10^6$ cm^{-3}.

Combined in Figure 10 are experimental data from our experiments, *Pichavant et al.* [2013] and *Yoshimura and Nakamura* [2010] demonstrate that the two types of dynamic dehydration differ significantly from the equilibrium predictions shown in Figure 1. As our scaling analysis showed, slower diffusion of CO_2 than H_2O may be important on realistic time scales for magma flushing. Our assumption about the same size of the spherical shell of the melt for all bubbles, used in numerical simulation, ignores the uneven distribution of bubbles in the melt volume and their possible escape. These effects are reflected in our data for run a21, where the composition point are scattered over a wide range of CO_2 and H_2O contents and do not follow a single trend.

All this makes it difficult to interpret the data on the content of CO2 and H2O in MIs. In general, the CO2 flushing model can be supported by the presence of low (near zero) CO2 and high H2O points on the diagram, which may represent the melt composition before CO2 influx. However, such compositions are rare, for example, in Figure 1 data for HRT MIs does not have distinct points ща both low and high water with low CO2. Almost CO2 free and water saturated compositions can also be produced at a high degree of magma crystallization with an exsolved

fluid accumulating CO2 [*Wallace et al., 1995*]. The interpretation of MI data is further complicated by the possible loss of water after entrainment. Taking into account the isotopic fractionation of fluid-mobile components between the fluid and the melt can be a decisive argument. A correlation between CO2 concentration and $\delta^{11}B$, $\delta^{7}Li$, $\delta^{34}S$ is expected if these components are extracted from the melt by a CO2-enriched fluid along with H2O.

Conclusions

1) Numerical modeling of the exchange of volatiles and the growth of a CO_2 bubble in a hydrous silicic melt is performed. It is demonstrated that water distribution between neighboring bubbles becomes uniform over a time equal to $\approx 0.14W^2/D_w$, where W is an inter-bubble distance, D_w is water diffusion coefficient and occurs when the melt is still undesaturated with CO_2.
2) Experiments with albite melt with an initial water content of about 5 wt.% at P=200 MPa and T=950°C showed that the initial content of CO_2 bubbles, with characteristic radii of tens of microns, reduces from to ~40 to 13 vol.% in 40 minutes due to the bubble escape. Flushing of the melt with mm-size CO_2 bubbles leads to uneven dehydration with a decrease in water content to 1.8-4.1 wt.%. The CO_2 concentration measured with μ-FTIR is 200-500 ppm, in general is below the saturation.
3) In a partially dehydrated melt rapid crystallization of albite with the release of volatiles is observed after 40 min, whereas the volume fraction of crystals increases to 70 vol.% in 4 hours. The estimated concentration of water in the residual melt approaches the maximum value of 2.5-2.8 wt.% close to the limit required for melt-crystal equilibrium under the experimental PT conditions.
4) Series of experiments on the exchange of volatiles between the CO_2 fluid and the hydrous albite melt through a discrete interface were performed at T=1020 ^{o}C and P=200 MPa. In these experiments, the linear scale of the diffusion process increased to several millimeters. The measured content of water and CO_2 at the interface is 2 wt.% and 200 ppm, respectively, which significantly exceeds the value imposed by fluid-melt exchange. We explain this by the formation of a SiO_2 rich protective film on the contact due to the preferential dissolution of Na_2O and Al_2O_3 in the carbonic fluid. Diffusion profiles in glass were measured using EMPA (H_2O) and μ-FTIR (H_2O and CO_2). The diffusion coefficients of H_2O (1.1×10^{-6} cm^2/s) and CO_2 (1.5×10^{-7} cm^2/s) obtained by fit of these profiles agree with the published data.

5) Possible episodes of interaction (flushing) of CO_2 enriched fluid and hydrous silicic magma will produce melts with dissolved CO_2 and H_2O contents following a distinctive trend. Due to the slow diffusion mobility of CO_2, the melt will first be dehydrated and then enriched with CO_2, which will be reflected in the composition of melt inclusions in quartz.

Acknowledgements. Authors thank for invaluable contribution of A.N. Nekrasov in EMPA analyses of our experimental samples and G.V. Bondarenko for assistance in the Raman investigation of the bubbles.

References.

1. A. Acosta-Vigil, D. London, G. B. Morgan and T. A. Dewers, Dissolution of Quartz, Albite, and Orthoclase in H2O-Saturated Haplogranitic Melt at 800°C and 200 MPa: Diffusive Transport Properties of Granitic Melts at Crustal Anatectic Conditions, in Journal of Petrology, vol. 47, no. 2, pp. 231-254, Feb. 2006, doi: 10.1093/petrology/egi073.

2. Barry, P.H., Hilton, D.R., Furi, E., S.A. Halldorsson, and K. Gronvold, Carbon isotope and abundance systematics of Icelandic geothermal gases, fluids and subglacial basalts with implications for mantle plume-related CO_2 fluxes, *Geochimica et Cosmochimica Acta*, 134, 74–99, 2014.

3. Berkesi, M., Guzmics, T., Szabó, C., Dubessy, J., Bodnar, R. J., K. Hidas, and K. Ratter, The role of CO_2-rich fluids in trace element transport and metasomatism in the lithospheric mantle beneath the Central Pannonian Basin, Hungary, based on fluid inclusions in mantle xenoliths, *Earth and Planetary Science Letters*, 331–332, 8–20, 2012.

4. Befus, K.S., Gardner, J.E. Magma storage and evolution of the most recent effusive and explosive eruptions from Yellowstone Caldera. Contrib Mineral Petrol 171, 30 (2016). https://doi.org/10.1007/s00410-016-1244-x

5. Befus, K.S., and M. Manga, Supereruption quartz crystals and the hollow reentrants Supereruption quartz crystals and the hollow reentrants, *Geology*, 47, 710–714, 2019.

6. Behrens, H., Ar, CO_2 and H_2O diffusion in silica glasses at 2 kbar pressure, *Chemical Geology,* 272, 40–48, 2010.

7. Behrens, H., Romano C., Nowak, M., F. Holtz, and D.B. Dingwell, Near-infrared spectroscopic determination of water species glasses of the system MAlSi,O, (M = Li, Na, K): an interlaboratory study, *Chemical Geology*, I28, 41–63, 1996.

8. Botcharnikov, R., Freise, M., F. Holtz, and H. Behrens, Solubility of C-O-H mixtures in natural melts: new experimental data and application range of recent models, *Annals of Geophysics*, 48(4/5), 633–646, 2005.

9. Caricchi, L., T. E. Sheldrake, and J. Blundy, Modulation of magmatic processes by CO_2 flushing, *Earth and Planetary Science Letters,* 491,160–171, 2018.

10. Cheng A.H.D., Golberg, M.A., E.J. Kansa, and G. Zammito, Exponential Convergence and H-c Multiquadric Collocation Method for Partial Differential Equations, *Methods in Partial Differential Equations*, 19, 571–594, 2003

11. Coenen,, K., Gallucci, F., Mezar, B., E. Hensen, and M.S. Annaland, An in-situ IR study on the adsorption of CO_2 and H_2O on hydrotalcites, *Journal of CO_2 Utilization*, 24, 228–239, 2018.

12. Couch, S., Sparks, R.S.J., Carroll, M.R. The Kinetics of Degassing-Induced Crystallization at Soufrière Hills Volcano, Montserrat, Journal of Petrology, 44(8), 2003, 1477–1502, https://doi.org/10.1093/petrology/44.8.1477

13. Coumans, J.P., Llewellin, E.W., Wadsworth, F.B., Humphreys, M.C.S., Mathias, S.A., B.M. Yelverton, and J.E. Gardner, An experimentally validated numerical model for bubble growth in magma, *Journal of Volcanology and Geothermal Research*, 402, 107002, 2020

14. Dallai, L., Cioni, R., C. Boschi, and C. D'Oriano, Carbonate-derived CO_2 purging magma at depth: Influence on the eruptive activity of Somma-Vesuvius, Italy, *Earth and Planetary Science Letters*, 310(1–2), 84–95, 2011.

15. Frezzotti, M. and J.L.R. Touret, CO_2, carbonate-rich melts, and brines in the mantle, *Geoscience Frontiers*, 5, 697–710, 2014.

16. Frezzotti, M., A. Peccerillo, and G. Panza, Earth's CO_2 degassing in Italy. In: (Eds.) Marco Beltrando, Angelo Peccerillo, Massimo Mattei, Sandro Conticelli, and Carlo Doglioni, *The Geology of Italy: tectonics and life along plate margins. Journal of the Virtual Explorer*, Electronic Edition, ISSN 1441-8142, 36, 21, doi:10.3809/jvirtex.2010.00227, 2010.

17. Gurenko A.A. (2021) Origin of sulphur in relation to silicate-sulphide immiscibility in Tolbachik primitive arc magma (Kamchatka, Russia): Insights from sulphur and boron isotopes. Chemical Geology 576, 120244.

18. Hidas, K., Guzmics, T., Szabó, C., Kovács I., Bodnar, R.J., Zajacz, Z., Nédli, Z., L. Vaccari, and A. Perucchi, Coexisting silicate melt inclusions and H_2O-bearing, CO_2-rich fluid inclusions in mantle peridotite xenoliths from the Carpathian–Pannonian region (central Hungary), *Chemical Geology,* 274(1–2), 1–18, 2010.

19. Holland, T. and R. Powell, Calculation of phase relations involving haplogranitic melts using an internally consistent thermodynamic dataset, *Journal of Petrology* ,42(4), 673–683, 2001.

20. Hui, H. and Y. Zhang, Toward a general viscosity equation for natural anhydrous and hydrous silicate melts, *Geochimica et Cosmochimica Acta*, 71, 403–416, 2007.

21. Kerrick, D.M. and G.K. Jacobs, A modified Redlich-Kwong equation of state for H_2O, CO_2, and H_2O–CO_2 mixtures at elevated pressures and temperatures*, American Journal of Science,* 281, 735–767, 1981.

22. King, P.L. and J.R. Holloway, CO2 solubility and speciation in intermediate (andesitic) melts: The role of H_2O and composition, *Geochimica et Cosmochimica Acta,* 66(9), 1627–1640, 2002.

23. Konschak, A. and H. Keppler, The speciation of carbon dioxide in silicate melts. , *Contributions to Mineralogy and Petrology*, 167(998), 2014.

24. Longpré, M.A., Stix, J., Klügel, A., and N. Shimizu, Mantle to surface degassing of carbon- and sulfur-rich alkaline magma at El Hierro, Canary Islands, *Earth and Planetary Science Letters*, 460, 268–280, 2017.

25. Lowenstern, J.B., and S. Hurwitz, Monitoring a Supervolcano in repose: Heat and volatile flux at the Yellowstone caldera, *Elements*, 4, 35–40, 2008.

26. M.L. Myers, Paul J. Wallace, Colin J.N. Wilson, Beth K. Morter, Elliot J. Swallow, Prolonged ascent and episodic venting of discrete magma batches at the onset of the Huckleberry Ridge supereruption, Yellowstone, Earth and Planetary Science Letters, 451, 2016, 285-297, https://doi.org/10.1016/j.epsl.2016.07.023

27. Mollo, S., Gaeta, M., Freda, C., Di Rocco, T., V. Misiti, and P. Scarlato, Carbonate assimilation in magmas: a reappraisal based on experimental petrology, *Lithos,* 114, 503–514, 2010.

28. Narine, S.S., K.L. Humphrey, and L. Bouzidi, Modification of the Avrami model for application to the kinetics of the melt crystallization of lipids, *Journal of the American Oil Chemists' Society*, 83(11), 913–920, 2006.

29. Navon, O., A. Chekhmir, and V. Lyakhovsky, Bubble growth in highly viscous melts: theory, experiments, and autoexplosivity of dome lavas, *Earth and Planetary Science Letters*, 160, 763–776, 1998.

30. Neukampf J., O. Laurent, P. Tollan, A.-S. Bouvier, T. Magna, P. Ulmer, L. France, B. S. Ellis, O. Bachmann (2022) Degassing from magma reservoir to eruption in silicic systems: The Li elemental

and isotopic record from rhyolitic melt inclusions and host quartz in a Yellowstone rhyolite, Geochimica et Cosmochimica Acta, 326, 56-76.

31. Newman, S., and J.B. Lowenstern, VolatileCalc: A silicate melt–H_2O–CO_2 solution model written in visual basic for excel, *Computers and Geosciences*, 28, 597–604, 2002.

32. Pichavant, M., Di Carlo, I., Rotolo, S.G., Scaillet, B., Burgisser, A., Le Gall, N., and C. Martel, Generation of CO_2-rich melts during basalt magma ascent and degassing, *Contributions to Mineralogy and Petrology,* 166, 545–561, 2013.

33. Ruefer, A.C., Befus, K.S., J.O. Thompson, and B.J. Andrews, Implications of multiple disequilibrium textures in quartz-hosted embayments, *Frontiers in Earth Science,* 9, 742895. doi: 10.3389/feart.2021.742895, 2021.

34. Rusiecka, M.K., and D.R. Baker, Growth and textural evolution during crystallization of quartz and feldspar in hydrous, rhyolitic melt, *Contributions to Mineralogy and Petrology*, 176(48), doi:10.1007/s00410-021-01809-1, 2021.

35. Simakin, A.G., and I.N. Bindeman, Convective melting and water behavior around magmatic-hydrothermal transition: numerical modeling with application to Krafla Volcano, Iceland, *Journal of Petrology*, 63(8), egac074, https://doi.org/10.1093/petrology/egac074, 2022

36. Simakin, A.G. and V.Y. Chevychelov, Experimental studies of feldspar crystallization of granite melts of varied water content, *Geokhimiya,* (2), 216–237, 1995.

37. Simakin, A.G., Armienti, P. & Epel'baum, M.B. (1999): Coupled degassing and crystallization: experimental study at continuous pressure drop, with application to volcanic bombs. *Bull. Volcanol*., **61**, 275-287.

38. Simakin, A.G., T.P. Salova, and G.V. Bondarenko, Experimental study of magmatic melt oxidation by CO_2, *Petrology*, 20(7), 593–606, 2012.

39. Simakin, A.G. and A. Ghassemi, Mechanics of magma chamber with implication to the effect of CO2 fluxing, *Chapter 9 in book "Volcanoes"*, Ed. G.Aiello, IntechOpen, 175–207, 2018.

40. Simakin, A.G., and V.N. Devyatova, Crystallization of Cpx in the Ab-Di System under the oscillating temperature: contrast dynamic modes at different periods of oscillation *Advances in Experimental and Genetic Mineralogy*, Springer, 97–120, 2020.

41. Stolper, E.M., Fine, G., T. Johnson, and S. Newman, Solubility of carbon dioxide in albitic melt, *American Mineralogist*, 72, 1071–1085, 1987.

42. S.E. Swanson, P.M. Fenn; Quartz crystallization in igneous rocks. American Mineralogist 1986; 71 (3-4): 331–342.

43. Wallace, P.J., Anderson, A.T., Jr., and Davis, A.M., 1995, Quantification of pre-eruptive exsolved gas contents in silicic magmas: Nature, v. 377, p. 612–616.

44. Wang, X., Chou, I.M., Hu, W., Burruss, R.C., Q. Sun, and Y. Song, Raman spectroscopic measurements of CO2 density: Experimental calibration with high-pressure optical cell (HPOC) and fused silica capillary capsule (FSCC) with application to fluid inclusion observations, *Geochimica et Cosmochimica Acta,* 75, 4080–4093, 2011.

45. Werner, C., and S. Brantley, CO2 emissions from the Yellowstone volcanic system, *Geochemistry Geophysics Geosystems,* 4(7), 1061, doi:10.1029/2002GC000473, 2003.

46. Yamamoto, J., and H. Kagi Extended micro-raman densimeter for CO2 applicable to mantle-originated fluid inclusions, *Chemistry Letters,* 35, 6, 610–611, 2006.

47. Yinnon, H., and D.R. Uhlmann, Applications of thermoanalytical techniques to the study of crystallization kinetics in glass-forming liquids, Part I: Theory, *Journal of Non-Crystalline Solids,* 54, 253–275, 1983.

48. Yoshimura, S., and M. Nakamura, Chemically driven growth and resorption of bubbles in amultivolatile magmatic system, *Chemical Geology*, 276, 18–28, 2010.

49. Zanotto, E., and D. Cassar, The microscopic origin of the extreme glass-forming ability of Albite and B2O3, *Sci Rep*, 7, 43022 https://doi.org/10.1038/srep43022, 2017.

50. Zelenski, M., Simakin, A., Taran, Yu., V.S. Kamenetsky, and N. Malik, Partitioning of elements between high-temperature, low-density aqueous fluid and silicate melt as derived from volcanic gas geochemistry, *Geochimica et Cosmochimica Acta*, 295, 112–134, 2021.

51. Zelenski M.; Kamenetsky,V.S.; Nekrylov, N.; Kontonikas-Charos (2022) A. High Sulfur in Primitive Arc Magmas, Its Origin and Implications. Minerals, 12, 37. https://doi.org/10.3390/min12010037

52. Zhang, Y., and H. Ni, Diffusion of H, C, and O components in silicate melts, *Reviews in Mineralogy and Geochemistry,* 72, 171–225, 2010.

Figures

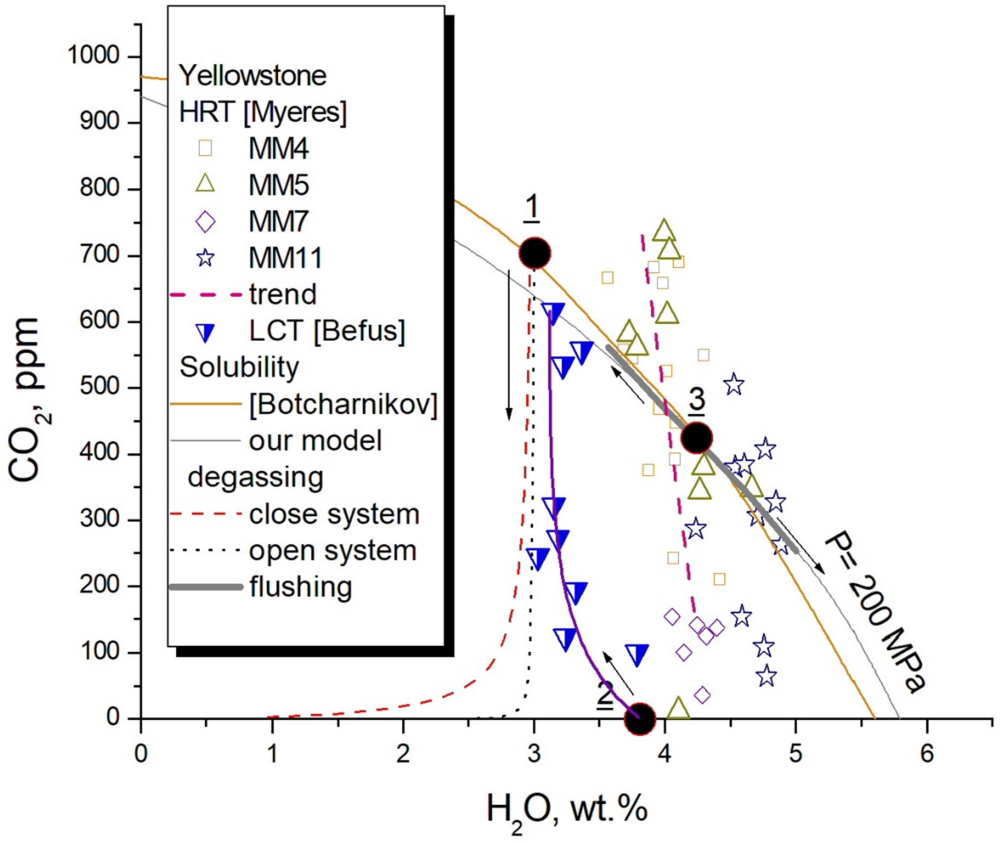

Figure 1. Compositions of melt inclusions in quartz from climatic eruptions of Yellowstone: Huckleberry Ridge Tuff (HRT), numbering of the different levels in the ash pile and analysis results from [*Myers et al., 2016*], Lava Creek Tuff (LCT) data from [*Befus and Gardner, 2016*]. The decompression degassing lines (open and close system modes are depicted by dotted and dashed lines, respectively) were calculated and marked with an arrow pointing down. The line of flushing with CO_2 enriched fluid is shown as a solid line marked with an upward arrow, schematically. Evolution of the melt composition in equilibrium at flushing (marked with arrow directed towards increasing CO_2 content) and crystallization (marked with arrow directed to increasing H_2O content) is plotted with thick grey line as part of solubility isobar at P=200 MPa. Ideal compositions of the starting melt are marked with solid circles (1- decompression degassing, 2 – dynamic flushing, 3- equilibrium flushing or fluid exsolution at crystallization).

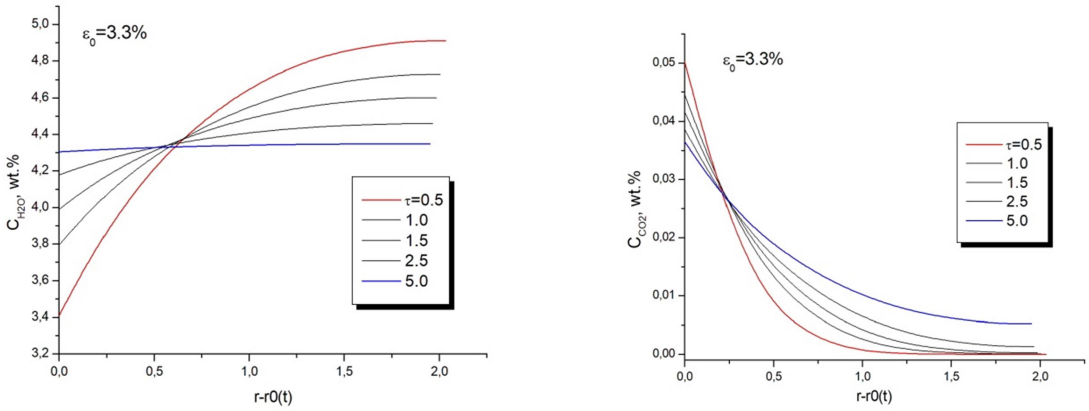

Figure 2. Concentrations of CO_2 and H_2O in the melt at the contact with the a CO_2 bubble in the hydrous melt. Calculations using Equations (1,5,6) at different moments of time (see legend). The distance from the contact is normalized to the initial bubble radius R_0, the time is scaled to the water diffusion time $\tau_0=R_0^2/D_{H2O}$, the initial water content is set at 5 wt.%. The linear dimensions of the bubble and melt shell correspond to the initial volumetric content of CO_2 fluid of 3.3 vol.%. See text for details.

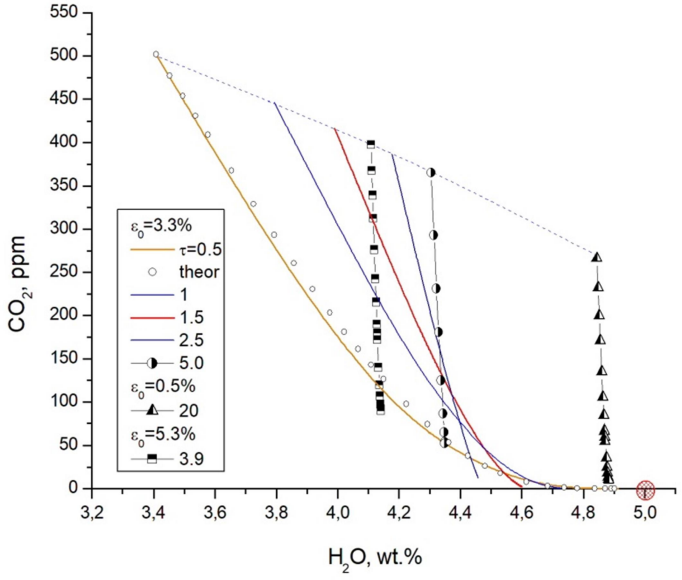

Figure 3. Calculated distributions of CO_2 and H_2O concentrations in the melt at the contact with the CO_2 bubble projected on the H_2O-CO_2 plot. The time intervals are shown in the legend (see Figure 1 for time scaling). The distributions are calculated for three volume fractions of the bubbles. The final distributions (symbols) of water and of CO_2 are, respectively, almost uniform and highly uneven. The points with the highest CO_2 content are on the fluid saturation curve (dotted line) and correspond to the fluid-melt contact. It takes more time to achieve a uniform distribution of water with a lower volume fraction of bubbles. The initial melt composition is shown by a hatched circle.

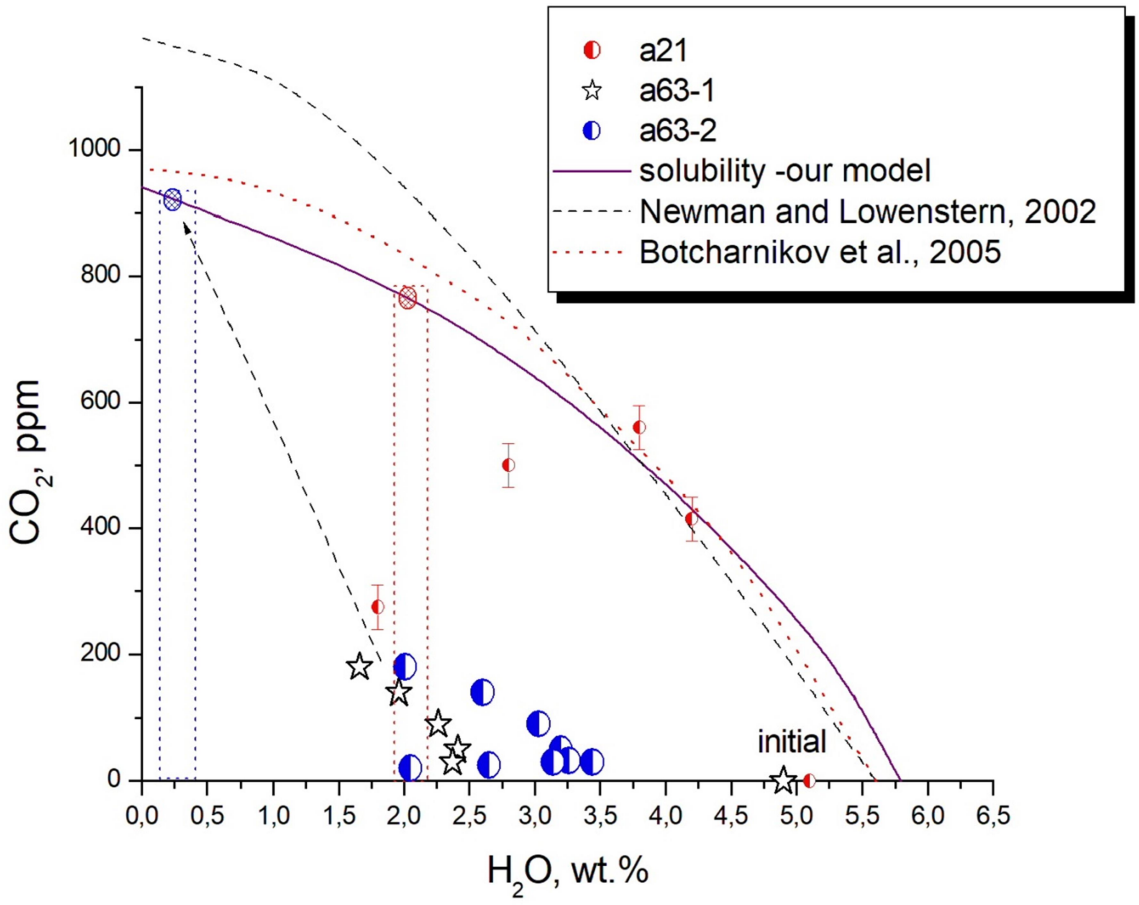

Figure 4. The results of our experiments on the composition of the fluid dissolved in the albite melt. Two profiles measured with μ-FTIR on two pieces of glass from the run a63 with frontal dehydration are represented with half-filled circles and open stars. Discreet points in the bubbly glass from the experiment a21 are marked with half-filled squares. The model solubility curve at 200 MPa and literature data are shown with lines. The equilibrium compositions for the exchange of the melt with CO_2 in the experiments are shown by hatched circles. The dotted boxes depict the expected locations of compositions homogenized with H_2O prior to homogenization with CO_2.

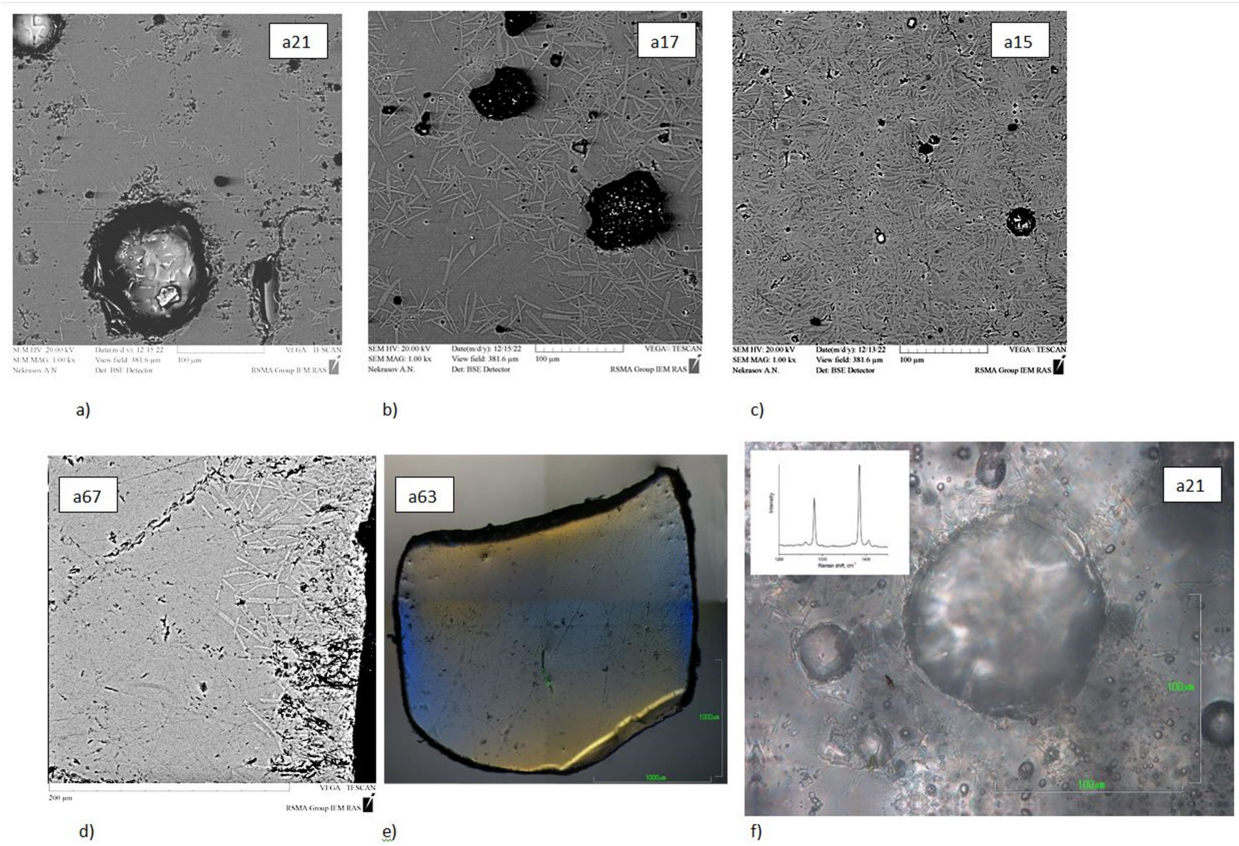

Figure 5. BSE (a-d) and optical (e,f) images of the experimental products, run numbers are indicated on the images. Images (a-c) show gradual increase in crystallinity and a decrease in the fluid bubbles fraction over time. d) In run a67 albite crystallization started from the capsule wall after dehydration of the melt near the contact. e) Double-polished glass plate used in μ-FTIR analysis. f) Optical image of the glass slice from run a21 (shortest duration 40 minutes) shows the presence of the small bubbles present in the starting imperfect glass, and larger bubbles rich in CO_2, reaching large size due to coalescence; Raman spectrum of CO_2 is in the inset.

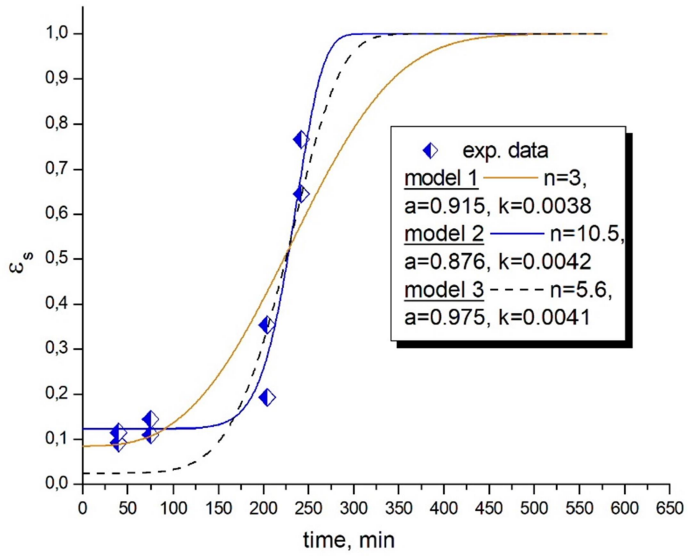

Figure 6. Time-dependence of the volume fraction of crystals in the bubble-free melt in the first series of experiments with starting albite glass powder. The experimental points (semi-filled diamonds) are approximated by the modified JMAK equation $\varepsilon_s = 1 - ae^{-k\,t^n}$ (see text) with the parameters indicated in the legend. The coefficient *a* is taken to be less than 1 to account for the rapid crystallization from the surface of glass fragments upon contact with CO_2 at the beginning of experiment. The classical model with n=3, implying kinetic control without nucleation, poorly fits the observations. The preferred model 2 with n≈10 implies rapid homogeneous nucleation with large delay time.

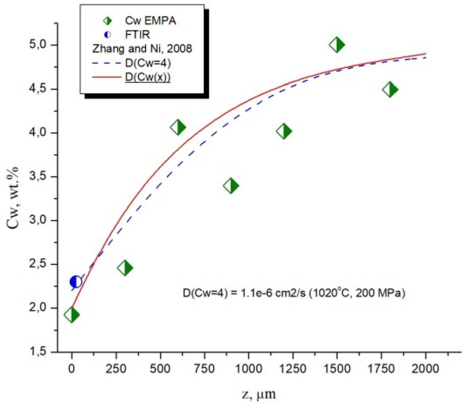

Figure 7. Water distribution in glass from experiment a57, demonstrating dehydration in contact with a CO_2-enriched fluid. Water concentrations were estimated with EMPA. Several theoretical profiles calculated with the parameters of the experiment a57 are shown; the diffusion profile at a constant boundary condition and diffusion coefficient calculated at a constant Cw= 4 wt.% is depicted by a dashed line; the profiles shown in solid lines are calculated with a diffusion coefficient dependent on water content [*Zhang and Ni, 2010*].

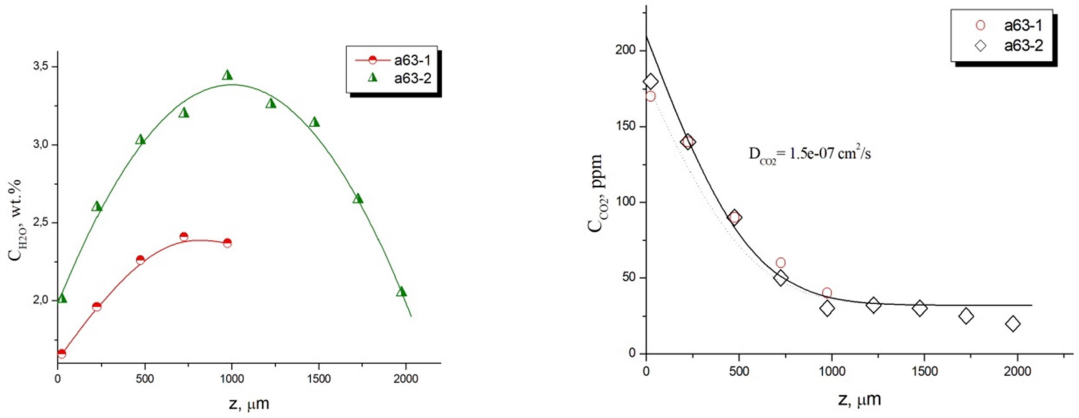

a) b)

Figure 8. The content of volatiles on two profiles across the glass from the run a63 from the top contact towards the bottom a) H_2O distributions for full (semi-filled triangles) and half (semi-filled circles) profiles b) CO_2 distributions and their approximation by a complementary error function (erfc), the value of the fitted diffusion coefficient is shown in the plot.

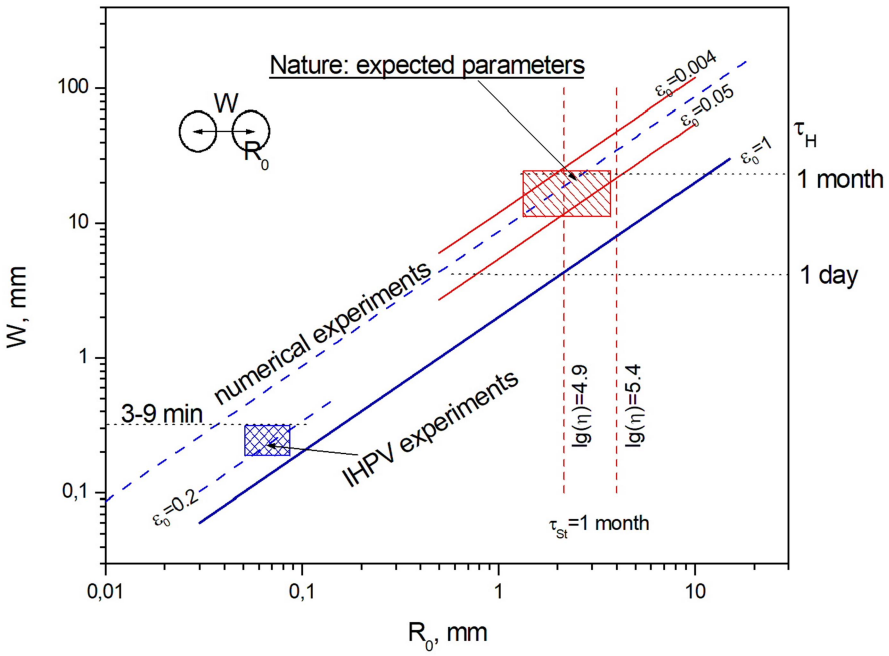

Figure 9. Schematic diagram showing the principle parameters of the CO_2 flushing process in our numerical modeling, experiments with albite melt and in nature. A homogeneous distribution of identical bubbles, the initial bubble radius R_0 and the inter-bubble distance W equal to $2R_1$ in the spherical shell model are assumed. The lines of the constant initial fraction of bubbles ε_0 are shown. The dashed lines show the average parameters of the numerical and IHPV experiments. Several values of water homogenization time $\tau_H=W^2/D_w$ are plotted near the vertical axis. For experiments with albite melt, the water diffusion coefficient D_w was calculated for Cw=1.5 and 4 wt.% at T=950°C, for natural rhyolite (τ_H values near the right axis) at Cw=4 wt.% and T=800°C. The vertical dashed lines correspond to the Stokes time τ_{St} = 1 month (see text) calculated for the albite melt with Cw=4 wt.% at T=800°C and rhyolite magma (larger values of viscosity and R_0) at the same parameters. For bubbles with $R_0 \leq$ 1 mm $\tau_{St} > \tau_H$ which means local equilibrium H_2O with melt and possible CO_2 unsaturation. In the experiments with albite melt, water and melt are expected to equilibrate on the scale $R_0 \approx 100$ μm.

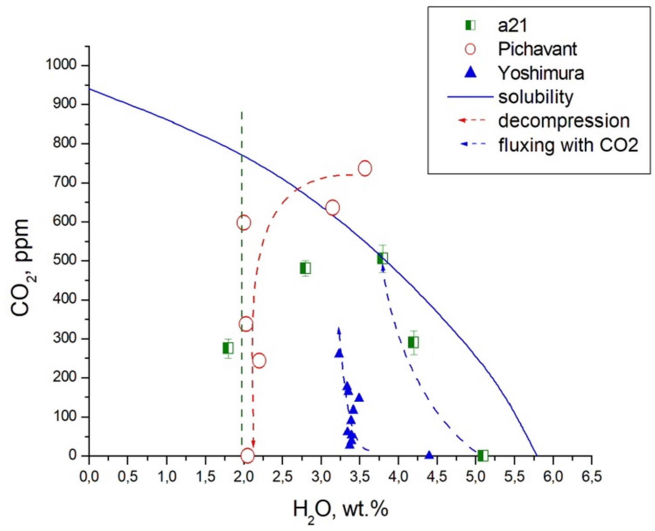

Figure 10. Diffusion-controlled trends in H_2O-CO_2 concentrations in the melt caused by CO_2 flushing and depressuration-induced vesiculation. The filled triangles display the profile distribution at the interface of the melt and CO_2 enriched fluid from [*Yoshimura and Nakamura, 2010*]. Partially filled squares refer to the experiment a21 with numerous CO_2 bubbles, the large data spread reflects uneven distribution of the bubbles in the melt with contrasting residence times. The vertical dahed line indicates the water content achieved with complete equilibration of the melt-fluid system without crystalllization. Open circles correspond to the experiment on vesiculation during depressurization of a basaltic melt saturated with CO_2-H_2O fluid at P=200 MPa from [*Pichavant et al., 2013*].

Table 1. Experiments on the interaction of albite melt with carbonic fluid

a) Series 1: initial water content 5.1 wt.%, T_{run}=950°C. P=200 MPa, glass powder

#	time, min	ε_{fl1},%	ε_{fl2}	ε_S,%	$C_{w,gl+s}$ (EMPA)	$C_{w,gl}$*	$C_{w,max}$ (T_{run})	$e_s \rightarrow 1$**			e_s=0***	
								$x_{CO2,min}$	$C_{w,eq}$	T_m,°C	$X_{co2,\ max}$	$C_{w,eq}$
A21	40	9.9	3.5	8-10	2.5±0.4	2.7	3.5	0.66	2.80	1008	0.77	2.15
A20	75	7.0	2.6	10-13	2.7±0.2	3.1		0.67	2.74	1011	0.78	2.11
A17	204	5.5	1.2	18-33	2.7±0.7	3.6		0.70	2.57	1021	0.79	2.00
A15	242	0.7	0.1	64-76	2.5±0.4	-		0.71	2.51	1024	0.80	1.96

b) Series 2: initial water content 4.9 wt.%, P=200 MPa, single glass piece

#	time, min	T_{run}, °C	Cw near contact		$C_{w,max}(T_{run})$	$e_s \rightarrow 1$**		
			EMPA	IR		$x_{CO2,min}$	$C_{w,eq}$	$T_m(C_{w,eq})$,°C
A57	53	1020	2.0	2.2	2.43	0.97	0.2	1149
A63	108	1020	1.8	2.0 (1.7)	2.43	0.98		
A67	239	975	2.0±0.1	-	3.09	0.98		

* Cw,gl is an estimate of water content in the interstitial glass equal to $Cw_{gl+s}/(1-\varepsilon_S)$ (average values of parameters are used), $C_{w,max}(T_{run})$ is liquidus water content at $T=T_{run}$,** parameters at almost full albite crystallization: $X_{CO2,min}$ – fluid composition, $C_{w,eq}$ is corresponding equilibrium water content in the melt, T_m liquidus temperature at given $C_{w,eq}$, *** equilibrium parameters of exchange without crystallization: fluid composition and water content in the melt.